TU Delft

Delft University of Technology

Wake scaling of actuator discs in different aspect ratios

Huang, Ming; Ferreira, Carlos; Sciacchitano, Andrea; Scarano, Fulvio

DOI
10.1016/j.renene.2021.11.045

Publication date
2022

Document Version
Final published version

Published in
Renewable Energy

Citation (APA)
Huang, M., Ferreira, C., Sciacchitano, A., & Scarano, F. (2022). Wake scaling of actuator discs in different aspect ratios. *Renewable Energy*, *183*, 866-876. https://doi.org/10.1016/j.renene.2021.11.045

Important note
To cite this publication, please use the final published version (if applicable).
Please check the document version above.

Copyright
Other than for strictly personal use, it is not permitted to download, forward or distribute the text or part of it, without the consent of the author(s) and/or copyright holder(s), unless the work is under an open content license such as Creative Commons.

Takedown policy
Please contact us and provide details if you believe this document breaches copyrights.
We will remove access to the work immediately and investigate your claim.

This work is downloaded from Delft University of Technology.
For technical reasons the number of authors shown on this cover page is limited to a maximum of 10.

Renewable Energy 183 (2022) 866–876

Contents lists available at ScienceDirect

Renewable Energy

journal homepage: www.elsevier.com/locate/renene

Wake scaling of actuator discs in different aspect ratios

Ming Huang *, Carlos Ferreira , Andrea Sciacchitano , Fulvio Scarano

Faculty of Aerospace Engineering, Delft University of Technology, Kluyverweg 1, 2629 HS, Delft, the Netherlands

ARTICLE INFO

Article history:
Received 11 June 2021
Received in revised form
9 November 2021
Accepted 11 November 2021
Available online 18 November 2021

Keywords:
Actuator disc
Wake scaling
Momentum recovery
Vertical axis wind turbine

ABSTRACT

The wake recovery from planar porous actuators that surrogate the effect of wind turbines is investigated, focusing on rectangular shapes for vertical axis wind turbines (VAWTs). We proposed an effective mixing diameter D^* to scale the streamwise momentum recovery for actuators of arbitrary shape. The length-scale D^* is given by the ratio between frontal area and disc perimeter characterising the wake-freestream interface, whereby the momentum loss and the turbulent exchange of momentum take place. Wind tunnel experiments of planar actuators from porous plates are presented. The three-dimensional development of the wake is surveyed up to six widths/diameters downstream of the actuators making use of robotic particle image velocimetry with helium-filled soap bubbles as flow tracers. The recovery rate analysis is performed using D^* for wake normalisation. The scaled wake data agrees well among actuators in different shapes. And it is significantly improved for rectangular actuators, comparing with existing scaling lengths. The flow behaviour is confirmed with numerical simulations of VAWT wakes with different aspect ratios, indicating the validity of this scaling concept for wind turbine wake modelling.

© 2021 The Authors. Published by Elsevier Ltd. This is an open access article under the CC BY license (http://creativecommons.org/licenses/by/4.0/).

1. Introduction

Porous plates have become prevailing representatives of horizontal axis wind turbines (HAWTs) to efficiently simulate wind farm behaviour by experiments [1]. In this context, a porous plate is often referred to as an actuator disc. As a result, investigations of circular porous plate wake can be found extensively in the literature [2,3]. In particular, Lignarolo et al. [4] shows that these devices reproduce key aerodynamic parameters such as velocity, pressure, and enthalpy fields, provided that the thrust coefficient is matched with that of wind turbines. Very recently, Helvig et al. [5], compared the near wake of porous plates against a lab-scale HAWT model. They concluded that a porous plate model mimics satisfactorily the mean flow properties, albeit the instantaneous pattern of unsteady vortices is substantially different.

The flow development across a porous plate is characterised by its porosity [6,7] and shape [8–10]. The former generally determines the drag coefficient, while the latter leads to a distinct flow pattern in its wake. Compared with solid plates, the flow at high porosity features less vortex shedding effect and the wake width is smaller and well approximated by the plate cross-section, so as HAWTs [4]. These features make porous plates a suitable and significantly simpler surrogate of wind turbines.

The idea to replace a wind turbine by a porous plate stems from the actuator disc theory that forms the basis of most analytical models developed for wind turbine wakes [11], where the turbine is treated as a stationary, permeable disc. Combined with the assumed self-similar behaviour of HAWT wakes in the far field, the velocity field can be predicted with relatively simple kinematic models [12,13], despite the complexity of the aerodynamic phenomena involved in the spatial development of the wake. The models from Jensen [14] and Larsen [15] are the most popular among the early works, followed by more recent advancements from Bastankhah and Porté-Agel [16] (BPA).

These models are formulated under different scaling laws, which describe the relation between the wake width δ, the centreline velocity deficit Δu_c and downstream position x (Fig. 1-top). The Jensen model assumes that δ expands linearly with x: $\delta(x)/D \propto x/D$, the normalised streamwise velocity deficit is expressed in terms of an empirical function of the downstream position: $\Delta u_c / U_\infty \propto (x/D)^{-2}$, where D is the wind turbine rotor diameter and U_∞ is the free stream velocity. In contrast, the Larsen model follows the scaling law for a fully developed turbulent wake [17]: $\delta(x)/\theta \propto (x/\theta)^{1/3}$, $\Delta u_c(x)/U_\infty \propto (x/\theta)^{-2/3}$, where θ is the momentum thickness, and is assumed to be equal to the rotor diameter

* Corresponding author. Faculty of Aerospace Engineering, Delft University of Technology, Kluyverweg 1, 2629 HS, Delft, the Netherlands.
E-mail address: M.Huang-1@tudelft.nl (M. Huang).

https://doi.org/10.1016/j.renene.2021.11.045
0960-1481/© 2021 The Authors. Published by Elsevier Ltd. This is an open access article under the CC BY license (http://creativecommons.org/licenses/by/4.0/).

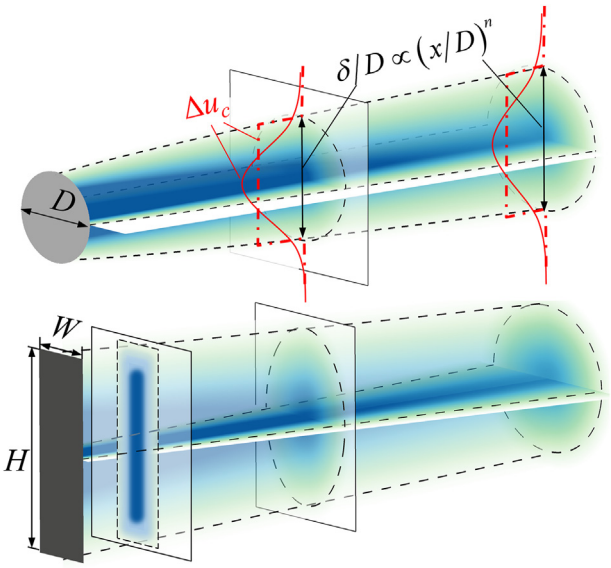

Fig. 1. Top: schematic representation of the wake of a circular actuator disc modelled with kinematic models, where the velocity distribution can be uniform (Jensen, red dash-dot lines) or continuous (BPA and Larsen, red solid lines). The exponent n denotes different scaling laws adopted (n = 1: Jensen and BPA, n = 1/3: Larsen); Bottom: transition to circular wake of a rectangular plate [9]. Colour-coded continuous momentum deficit (blue for high values, green for vanishing deficit) and plate type (light grey for permeable plate, dark grey for solid plate).

D in the wake model. The BPA model assumes a linear wake expansion as that of the Jensen model: $\delta(x)/D \propto x/D$, while δ is described as a function of the standard deviation σ of the momentum deficit distribution, assumed to be Gaussian.

Despite of the different hypotheses adopted, all the above models employ a proper streamwise distance normalisation to determine the velocity deficit evolution. As the circular actuator disc wake is deemed as circular-symmetric, the diameter D naturally becomes the normalisation length, connecting the wake deficit development and the actuator dimension.

However, it is less trivial to define the scaling length in the wake of a non-circular-symmetric actuator disc, specifically, a rectangular actuator with a variable aspect ratio (AR), which is the surrogate of vertical axis wind turbine [8]. In particular, no research is found in the literature comparing the momentum recoveries in the wakes of rectangular and circular porous plates. However, Fail et al. [9] measured the wake of a solid circular plate and rectangular ones with different ARs, shedding light on the different flow patterns in their wakes (Fig. 1-bottom). As illustrated, a transition from a rectangular to an elliptical and finally to a circular wake is observed. Length scales such as the height (H), the width (W), and a diameter after transition are involved in the wake shape characterisation, indicating that a proper scaling length should be given based on multiple feature lengths to adapt to such transition.

A consistent wake scaling length for rectangular actuators with different ARs is crucial for the formulation of kinematic wake models of VAWTs. Currently, a few rectangular-actuator-based kinematic wake models for VAWTs have been introduced as extrapolations of HAWT wake models (e.g., Refs. [18–20]. In these models, the turbine rotor height (H) and diameter (D, corresponding to W of rectangular actuators) are both employed for streamwise distance normalisation, under the assumption that an elliptical wake is imparted by the actuator, which preserves its shape and merely expands by turbulent diffusion. Such assumption preludes an inconsistency in the scaling of rectangular actuator's wake, because the latter transitions from an elliptical to a circular shape.

A survey in terms of wake scaling lengths for bluff-body/wind turbine with various frontal areas is discussed here. a) The width W (or diameter following the convention of wind turbine wake) is often used in the horizontal and vertical axis wind turbine wake normalisation [12,13], however, it leads to inconsistency when applied to elongated wake. b) Apart from the width, a characteristic length $l = A^{1/2}$ is widely documented in the literature for the wake normalisation of solid plates with different geometries, including circular, rectangular disc with various ARs, and etc. [9,21]. Here A denotes the frontal area, and l essentially corresponds to the side length of an equivalent square. c) Very recently, Shamsoddin and Porté-Agel [22] proposed an equivalent diameter $D_{eq} = (4A/\pi)^{1/2}$ for VAWT wake normalisation, based on the assumption that the wake of a VAWT with rectangular frontal area eventually (i.e. at some distance downstream) develops into a circular shape in the far wake (Fig. 1-bottom). D_{eq} is essentially an extrapolation of the momentum thickness concept for planar wakes, where the VAWT's momentum deficit is redistributed to an equivalent circular disc. Their results indicate that the momentum recovery normalised by D_{eq} exhibits a limited degree of match for large values of AR, within the typical inter-turbine separation distances of wind farms (e.g. from 3 to 8 diameters, [23]. Due to the same reason, W and l present inconsistencies as scaling lengths. Fig. 2 depicts a comparison among W, l, and D_{eq} normalisations for rectangular solid plates with various ARs. l and D_{eq} are incorporated in the same plot since they are almost equal except for a constant coefficient of $(4/\pi)^{1/2}$. The centreline velocity deficits are retrieved from Ref. [9]. Clearly, although l and D_{eq} performs better for moderate ARs, large discrepancies show up for AR = {5, 10} at $x/l < 4.5$ and $x/D_{eq} < 4$.

It is argued here that an additional physical constraint needs to be accounted for, which has not been considered in the above works: namely, the region of active mixing for the wake recovery of non-circular-symmetric actuators, which can largely differ from that of the equivalent circular disc. Therefore, the actuator perimeter by the wake, similar to the concept of "wetted perimeter" for flow in ducts of arbitrary cross-sectional shape, is expected to play a role in the rate of kinetic energy exchange and ultimately affect the momentum recovery. In the present work, this concept is first elaborated theoretically and supported by experiments and simulations.

The present work deals with frontal shape effects on the wake recovery rate, specifically for planar actuator discs with a variable AR that are adopted in existing kinematic wake models. The scaling of the resulting wake is discussed and an effective mixing length D^* for streamwise normalisation is proposed accounting for the shape effects supported by a theoretical derivation of the concept.

The experimental data is gathered with plates of uniform porosity as actuator discs. Actuators with circular, square and rectangular shape (AR = 3) are examined. Given the three-dimensional nature of the flow field, the velocity field

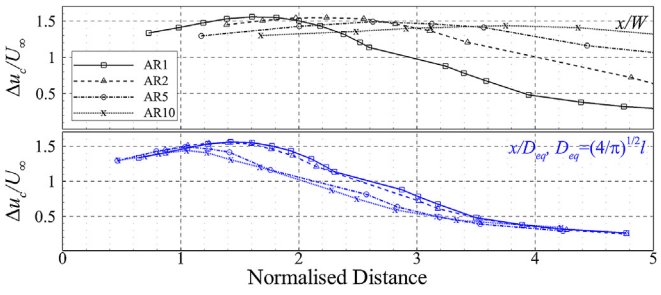

Fig. 2. Comparison of normalisation lengths (W, $D_{eq}(l)$) for centreline velocity deficits along x-direction. Wake data of rectangular solid plates with AR = {1, 2, 5, 10} are retrieved from Ref. [9].

measurements are conducted with the robotic volumetric particle image velocimetry (PIV) measurement technique [24]. The spatial distribution of the velocity enables the analysis of momentum deficit in the turbulent shear layer and wake recovery. The application scenario of D^* is extended to the wake of a VAWT in a set of numerical simulations based on unsteady Reynolds averaged Navier-Stokes equation (URANS) and actuator line model. The latter extends the range of AR up to 10 in the attempt to illustrate the asymptotic conditions for wake scaling.

2. Derivation of the effective mixing diameter, D^*

The momentum recovery and its relation with the shape of the actuator surface are modelled with a control volume (CV) approach. The CV is placed after the actuator surface; Its cross-section is chosen with the same shape and frontal area as the actuator (Fig. 3-left), the latter has a frontal area A and perimeter P. The definition of the CV is valid at locations where the shape effect is dominant and the expansion of the wake is less notable, usually it is in the near wake yet far enough away from the actuator. The CV also provides a straightforward estimation of the momentum past a hypothetical turbine, and follows the concept widely reported in the literature [25–27].

For sake of simplicity, the CV is placed sufficiently far from the actuator surface, such that the effect of the static pressure gradient in the equation of momentum conservation can be neglected. A top-hat velocity distribution along cross-sections is assumed, with streamwise velocity equal to U_∞ outside of the CV and to $U(x)$ inside the CV. Considering a portion of the CV with an infinitesimal streamwise length dx, the flow velocity at the upstream face of the CV is indicated with U, whereas it increases to $U + \mathrm{d}U$ at the downstream face. A cross flow velocity V, solely determined by the streamwise distance x, is presented to guarantee mass conservation (Fig. 3-left):

$$(U+\mathrm{d}U)A - UA - VP\mathrm{d}x = 0 \tag{1}$$

where the sign convention is that a vector pointing out of the CV is positive. And therefore,

$$V = \frac{A}{P}\frac{\mathrm{d}U}{\mathrm{d}x} \tag{2}$$

The frontal view of the present CV is shown in Fig. 3-right, which is a rectangular actuator (grey rectangle) with a cross-section area $A = W{\cdot}H$. As a comparison, other existing methods to simplify the actuator wake and obtain a normalisation length scale are also illustrated in Fig. 3-right, consisting of: a) an equivalent circular area of diameter $D_{eq} = (4A/\pi)^{1/2}$ (represented in blue); b) the square-equivalent actuator, represented in green, with length scale $l = A^{1/2}$. We draw here the attention to the perimeter of the actuator $P = 2W{+}2H$ and that of the area-equivalent shapes, namely $P_{eq} = \pi{\cdot}D_{eq}$ and $P_{sq} = 4l$ for the circular- and square-equivalent cases respectively. In both cases, the latter simplifications underestimate the actual perimeter of the rectangular actuator and in turn that of its wake.

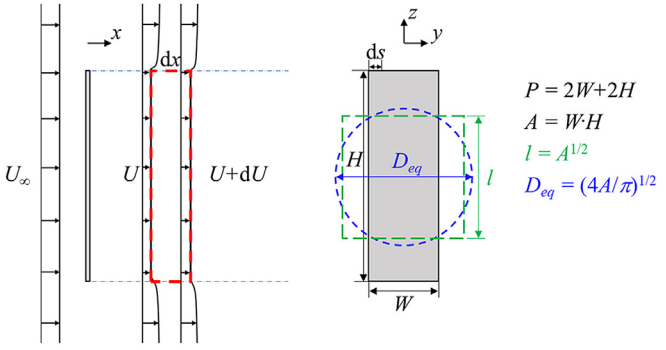

Fig. 3. Left: sketch of the actuator (grey rectangle) and relative control volume (red dashed rectangle) to formulate the wake momentum development; Right: front view of a rectangular actuator disc, with indicated perimeter P and area A, and illustration of equivalent shapes corresponding to existing normalisation methods (W, l, D_{eq}).

The momentum deficit caused by the actuator is assumed to be uniform over the cross-section, and the shear stress is uniformly distributed along the perimeter of the cross-section of the CV; The latter is assumed to be equal to the actuator perimeter. The recovery of the streamwise velocity (viz. momentum recovery) is treated as a sole function of the streamwise distance past the actuator. The aim of the present analysis is not only to account for the cross-sectional momentum deficit that occurs within the frontal area, but also introduce the momentum transport across the wake interface as a main driver for the process of momentum recovery. By this approach, a normalisation length can be obtained whereby the streamwise development of the momentum in the wake becomes independent of the actuator shape.

Consider the streamwise momentum balance in the CV:

$$\rho(U+\mathrm{d}U)^2A - \rho U^2A - \rho U_P V P\mathrm{d}x = \tau P\mathrm{d}x \tag{3}$$

where U_P is the streamwise velocity along the lateral interface of the free-stream and the wake bounded by the CV. It is assumed that $U < U_P < U_\infty$. The simplifications leading to the formulation in eq. (3) are of time-averaged analysis, where time derivatives are neglected. Moreover, body forces are absent and the pressure term is negligible. The shear stress τ is assumed to be uniformly distributed along the perimeter, yet evolving along the developing shear layer; As a result, τ solely depends upon the x-coordinate. Considering the assumptions, and combining with eq. (2), eq. (3) simplifies to:

$$2\rho U\mathrm{d}UA - \rho U_P A\mathrm{d}U = \tau P\mathrm{d}x \tag{4}$$

where $(\mathrm{d}U)^2$ is neglected compared with $2U\mathrm{d}U$. Thus, the rearranged expression

$$\frac{\mathrm{d}U}{\mathrm{d}x} = \frac{1}{\rho}\frac{P}{A}\frac{\tau}{2U-U_P} \tag{5}$$

indicates that the momentum recovery rate depends upon the ratio between cross-sectional area A and the wake perimeter P, in analogy with the concepts of wetted perimeter leading to the hydraulic diameter as originally introduced by Darcy [28]. The effective mixing diameter D^* is defined in the present context that normalises the averaged streamwise velocity recovery:

$$D^* = \frac{4A}{P} \tag{6}$$

Combining eqs. (5) and (6) one obtains:

$$\frac{\mathrm{d}U}{\mathrm{d}(x/D^*)} = \frac{4}{\rho}\frac{\tau}{2U-U_P}(x) \tag{7}$$

Eq. (7) indicates that, for an actuator with an arbitrary shape, the wake recovery rate along the streamwise distance normalised by D^* becomes shape independent. Specifically, for a highly elongated actuator, where $H \gg W$, $D^* \approx 2W$; for actuators with square cross-section ($H = W$), then $D^* = H = W$.

To verify the adequacy of the effective mixing diameter D^* as a generic scaling length for actuators of different shapes, and assess

until where the D^* works or not, a set of wake measurements from circular and rectangular actuator discs are carried out in this work. The experimental data is used to compare the use of D^* with the traditional choices of length scale such as width W and a characteristic length l alongside the recently introduced D_{eq}.

3. Experimental set-up

3.1. Wind tunnel and models

The experiments are conducted in the W-Tunnel of the TU Delft Aerospace Engineering Laboratories, a low-speed open-jet wind tunnel with exit cross-section of 0.6 × 0.6 m^2. The measurements are carried out at free stream velocity $U_\infty = 5$ ms^{-1} with a turbulence level rated to approximately 1%. The ground is not presented in the measurement.

Circular, square and rectangular porous plates are chosen to realise the actuator discs from perforated metal plates of 2 mm thickness, with uniformly distributed square holes (Fig. 4). The apertures in the plate are 8 mm wide and the pitch is 12 mm, yielding a porosity of 44%. At the chosen free stream velocity, the Reynolds number based on the model width attains 4×10^4 for circular and square plates, and 2×10^4 for the rectangular plate. The plate is installed at the wind tunnel exit and held by a circular rod of 10 mm diameter (Fig. 5). The properties of the actuators with different geometries are listed in Table 1.

3.2. Measurement systems and data processing

The aerodynamic drag produced by the plate and its support is measured by a load sensor based on strain gauges (KYOWA, type KFG-5-120-C1-23) applied to an aluminium strut. The strain on the strut is converted into a voltage signal.

The velocity field before and behind the actuator ($-1 < x/W < 6$) is measured by PIV. The overall measurement domain is covered using a robotic PIV system [24], based on the principle of coaxial volumetric velocimetry (CVV, [29]. The measurement system features four CMOS cameras installed in a compact tomographic arrangement (Fig. 5-left). Illumination is provided by a Quantronix *Darwin-Duo* laser (527 nm wavelength, 2 × 25 mJ pulse energy at 1 kHz). The light is transported through an optical fibre and propagates conically from the exit placed between the cameras. The resulting region of measurement has approximately 400 × 400 mm^2 cross-section at a 400 mm distance from the CVV head. Synchronisation of illumination and imaging is made with a LaVision programmable timing unit (PTU 9) controlled from a PC

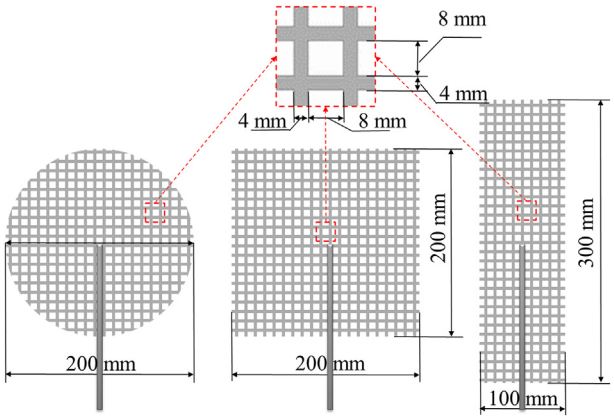

Fig. 4. Geometrical details of circular, square and rectangular porous plates.

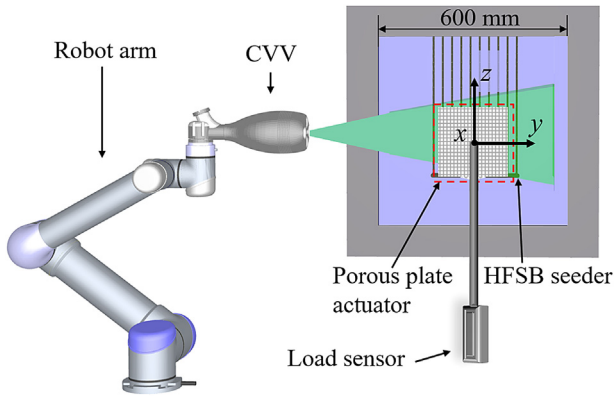

Fig. 5. Layout of experiments: wind tunnel and square actuator at its exit. Robotic arm and coaxial volumetric velocimeter, with an indication of measurement region.

Table 1
Geometrical parameters and equivalent length-scales of actuator discs.

Geometry	Area (cm^2)	Perimeter (cm)	W (D) (cm)	D_{eq} (cm)	D^* (cm)
Circle	314.2	62.8	20.0	20.0	20.0
Square	400.0	80.0	20.0	22.6	20.0
Rectangle	300.0	80.0	10.0	19.5	15.0

with the DaVis 10 software. Helium-filled soap bubbles (HFSB) are used as flow tracers. The HFSB have a mean diameter of 0.4 mm and the neutrally buoyant condition is met within approximately 10% [30]. HFSB are released in the wind tunnel settling chamber at a rate of approximately 5 × 10^6 bubbles/s yielding a concentration of 2 bubbles/cm^3.

The measurement views in the horizontal (x-y) and vertical (y-z) planes that compose the domain of interest are shown in Fig. 6. The robotic system points at 16 to 24 positions (instantaneous field of view, IFOV) for the circular/square and rectangular actuators, respectively. At each position, 5000 images are recorded at a rate of 789 Hz (measurement time of 6.3 s). The motion of the CVV system by the robotic arm is controlled using the RoboDK software. Image acquisition and storage require approximately 1 min for each measurement position.

Approximately 1200 particle tracks are captured in each recording. The raw images are pre-processed by a temporal high pass

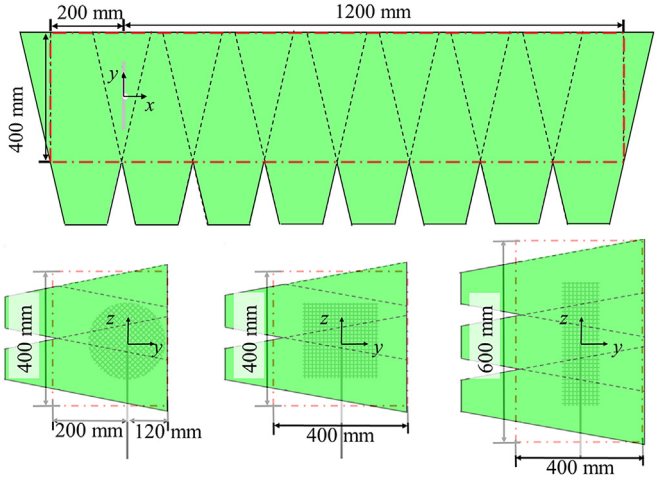

Fig. 6. Top- (up), and Front- (bottom) view of the porous plate (origin defined at the centre of the plate) and the IFOVs, the overall measurement domain is marked by the red dash-dot line.

filter (see Ref. [31] that eliminates unwanted background reflections. A sample of raw and pre-processed images is given in Fig. 7. The tracer velocity is obtained via Lagrangian Particle Tracking using the Shake-the-Box algorithm [32]. The measured instantaneous velocity vectors are defined at the scattered instantaneous positions of the tracers. The ensemble average velocity is evaluated within cubic cells (or bins) of 20 × 20 × 20 mm^3 volume, yielding the three-dimensional distribution of time-averaged velocity. Adjacent bins overlap by 75%, resulting in a Cartesian grid of velocity vectors with 5 mm pitch. The vorticity vector is evaluated by centred finite-difference of velocity values from neighbouring grid nodes.

3.3. Experimental uncertainty

The load sensor was calibrated within the force measurement range 0–1 N. A linear relation between measured voltage and corresponding force was evaluated using least squares regression; the standard uncertainty of the measured load induced by the actuators is 2.3% of the measured value.

The expanded uncertainty of the time-averaged streamwise velocity estimation U is determined as

$$\varepsilon_U = \frac{k\sigma_U}{U_\infty \sqrt{N}}, \tag{8}$$

where σ_U is the standard deviation of instantaneous velocity and $k = 2$ is the coverage factor for 95% confidence level. In the wake of the porous plates, σ_U attains typical values of about 0.2 m/s, corresponding to a turbulence intensity of 4%. The value of the number N of samples is in the order of 1000 in most of the measurement domain, although it can vary from 50 to 18,000, depending on the distance between the measurement location and the CVV head. The corresponding value of ε_U remains below 0.5% in most of the measurement domain. Higher turbulent intensity values (up to 25%) are encountered in the shear layers, leading to an increased uncertainty of the mean velocity, which locally reaches 2% of the free-stream velocity.

3.4. Spatial resolution effect

Given the bin size adopted for the robotic PIV measurements (20 × 20 × 20 mm^3), the velocity field reproduces the macroscopic behaviour of the flow around the actuator discs. A high-resolution planar PIV measurement (see appendix A) is employed to verify the applicability of using such PIV technique in measuring the wake of porous plates. Although the detailed behaviour of the flow across the orifices of the porous plates is not captured, the results of robotic PIV are in excellent agreement with the high-resolution planar data upstream of the plate and downstream of it after approximately 6 pore pitches, where the relative error of the velocity is approximately 1.3%.

4. Experimental results and discussion

4.1. Actuator thrust coefficient

The thrust coefficient, C_T is one of the inputs for the kinematic wake models examined in this work. C_T is defined as:

$$C_T = \frac{T}{\frac{1}{2}\rho U_\infty^2 A} \tag{9}$$

where T is the thrust force induced by the actuator to the fluid, that is the actuator's drag. The effect of the rod is accounted for with the following procedure: firstly, the loads with actuator attached (T_1) and unattached (T_2) to the supporting rod are measured, respectively; then T is evaluated as $T = T_1 - T_2$. ρ is the air density, U_∞ is the free stream velocity, and A is the frontal area of the actuator. The measured values and resulting relative errors of C_T of the different actuators are listed in Table 2. The resulting C_T are approximately the same within the measurement uncertainty, which confirms that C_T is little sensitive to the shape of the actuators. The chosen porosity results in $C_T \approx 0.89$, which is the point of optimal energy extraction according to the actuator disc model and Betz law [33]. This value of C_T is similar to that reported in the work of [34]; where the dynamic wake of a plate with the same porosity was investigated. Fig. 8 compares the relation between thrust and actuator porosity measured in this work (labelled “present data”) with measurements by other authors as reported in the work of [4,34]; the value of C_T measured in this work lies within the cluster of considered data.

4.2. Velocity field distribution

The contours of time-averaged streamwise velocity u from PIV measurements are discussed from Figs. 9–13, showing the overall

Table 2
Thrust measurements conditions and results.

	porosity	U_∞ [m/s]	ρ [kg/m^3]	T [N]	*CT*	ε_{C_T}
Circular	0.44	5.12	1.21	0.460	0.92	4.7%
Square	0.44	5.14	1.19	0.548	0.87	3.7%
Rectangular	0.44	5.15	1.19	0.444	0.93	4.9%

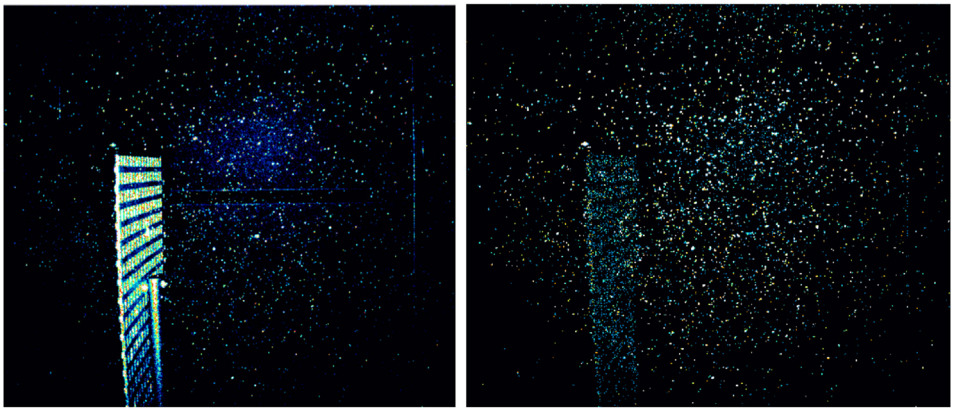

Fig. 7. Raw (left) and pre-processed (right) CVV images of HFSB tracers, with the square actuator surface in view.

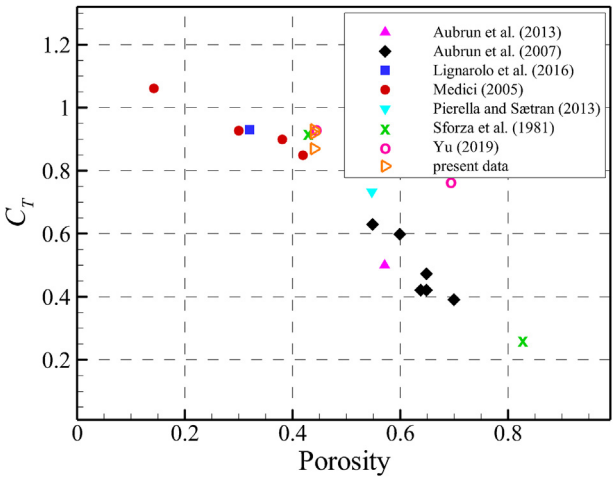

Fig. 8. Thrust coefficient as a function of porosity; comparison between current results and literature.

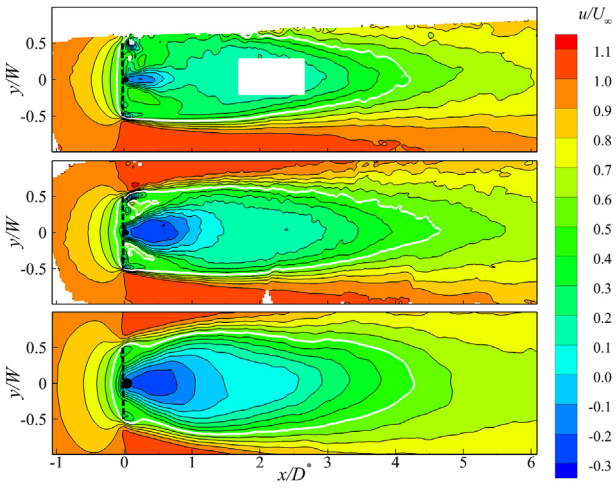

Fig. 9. Contours of normalised streamwise velocity (u/U_∞) in the x-y plane at $z/D = 0$. Circular (top), square (middle) and rectangular actuator (bottom). The white contour line represents the location where the wake velocity attains 50% of the free-stream value.

shape of the measurement results. In Figs. 9 and 10, the horizontal and vertical planes across the centre of the actuator surfaces are chosen for comparison, respectively. The x-coordinate, which points to the streamwise direction, is normalised by D^*, to examine the validity for normalising the streamwise momentum deficit recovery. Meanwhile, the length scale W, i.e., the diameter of the circular disc and the widths of the square or rectangular disc, is used for length normalisation in both lateral and spanwise directions, as widely adopted in the literature (e.g., Refs. [8,18,22]. This selection is to simply show the cross-sectional wake shape imparted by the actuators.

The velocity contours in the x-y plane (Fig. 9) illustrate the flow deceleration upstream caused by the adverse pressure gradient imposed by the actuator. The rectangle patch in the velocity contour of the circular actuator disc covers a region with relatively high measurement uncertainty, which was due to an accidently increased background reflection.

The circular and square plates impart a comparable deceleration, whereas the rectangular actuator yields a slightly higher deceleration upstream of the model. The latter is ascribed to the fundamental difference between the 3 dimensional and quasi-2-dimensional

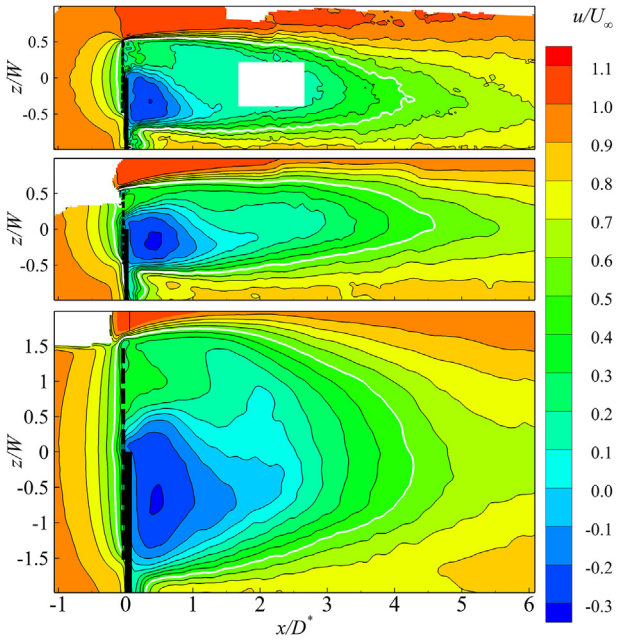

Fig. 10. Contours of normalised streamwise velocity (u/U_∞) in the x-z plane at $y/D = 0$. Circular (top), square (middle) and rectangular actuator (bottom).

condition of adverse pressure gradient associated with the AR of the rectangular actuator, where the scaling of the stagnation region is different from that of a circular-symmetric object.

Immediately downstream of the actuator, the most pronounced deficit is associated with the presence of the supporting rod, which also introduces local flow reversal. On the sides (e.g., $y/W = \pm 0.4$) one observes a velocity deficit past the grid of approximately 50%. This result compares favourably with the deficit of 40% reported in the work of [2]; where an actuator disc with a porosity of 55% was used.

For the circular actuator, a narrow recirculation region is found at about $x/W = 0.1$, whereas for the square and rectangular surfaces such recirculation region is significantly wider. This may be explained with the support rod blocking comparatively more perforated area in the cases of square and the rectangular plate, as shown in Fig. 4. The flow evolution along the symmetry axis confirms a smaller effect of the support for the circular actuator.

In order to assess the topology of the flow induced by the support, the velocity field in the x-z plane is shown in Fig. 10. The comparison indicates that the effect of the rod is not negligible within $1D^*$, as it causes a flow reversal up to u/U_∞ = - 0.2 in this region.

The normalisation of the streamwise direction with respect to D^* yields a good agreement among the contour lines in the wakes of the different actuators (see Figs. 9 and 10). Take the white contour lines as an example, where the mean streamwise velocity attains 50% of the free-stream value: they extend until around $x = 4.5D^*$ for all the cases. A more quantitative discussion about the validation of D^* for streamwise distance normalisation is presented in section 4.3.

The velocity distribution at different y-z cross-sections in the wakes of the three actuators is depicted in Figs. 11–13, respectively. For the position right after the actuator surfaces, namely when $x/D^* = 0.1$, the wakes feature the same shape as that of the actuator surfaces, but slightly expanded. Here the localised effect of the supporting rod is clear, inducing reverse flow up to - $0.2U_\infty$. As the wakes develop further downstream, their centres slightly shift downwards under the effect of the rod presence, as also reported in the literature [35,36]. The blue contour line indicates the shear layer shape development, which bounds a region with the equivalent

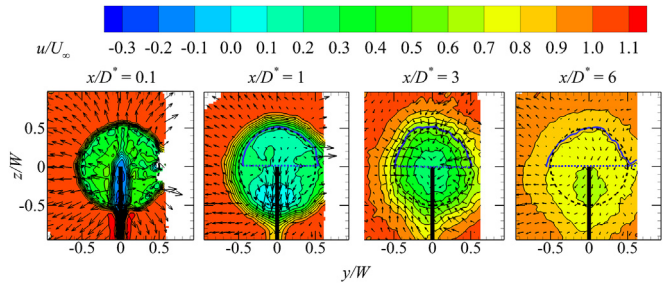

Fig. 11. Streamwise velocity contours and in-plane velocity vectors pattern at four cross-sections downstream of the circular actuator. The blue contour line together with the dashed line ($z = 0$) bounds half of the equivalent actuator frontal area and its length correspond to half of the wake cross-section perimeter (eq. (6)).

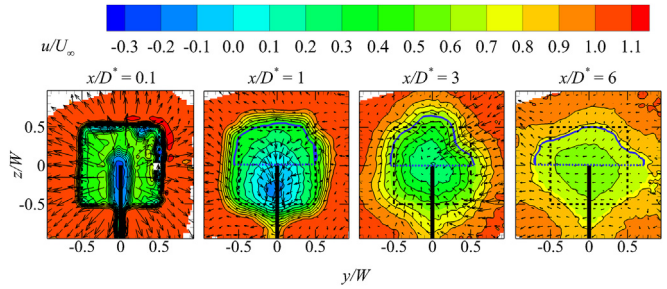

Fig. 12. Streamwise velocity contours and in-plane velocity vectors at cross-sections downstream of the square actuator. The blue contour line together with the dashed line ($z = 0$) bounds half of the equivalent actuator frontal area and its length correspond to half of the wake cross-section perimeter (eq. (6)).

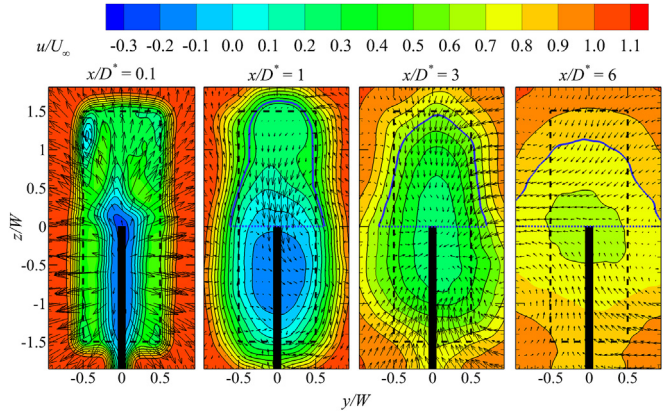

Fig. 13. Streamwise velocity contours and in-plane velocity vectors at cross-sections downstream of the rectangular actuator. The blue contour line together with the dashed line ($z = 0$) bounds half of the equivalent actuator frontal area and its length correspond to half of the wake cross-section perimeter (eq. (6)).

actuator frontal area (only the upper half, i.e., $z \geq 0$, is considered for area evaluation to avoid including the supporting rod effects).

The circular actuator produces a rather circular-symmetrical development of the deficit region. In contrast, the square actuator exhibits pronounced geometric modifications with the shear layer moving inwards at the corners. The latter is also reported in the work of Nedić et al. [37] for the wake of a solid square plate. This lower rate of expansion at the corners is ascribed to the onset of streamwise vortex-pairs that induce a cross-flow with resultant inward motions at the corners.

As a result, the streamwise velocity contour at $x/D^* = 1$ has already lost the sharp corners and the wake tends towards a cloverleaf shape. At the most downstream observation ($x/D^* = 6$), the region of momentum deficit has almost turned into a diamond shape. The rod effect is similar to that of the circular shape and vanishes by $x/D^* > 3$. Judging from the blue contour lines, the square actuator wake does not evolve into a circular wake within $6D^*$, and the perimeters of the equivalent regions keep close to the actuator perimeter.

The wake of the rectangular actuator features a similar trend to that of the square one, provided that the vertical elongation is taken into account. Judging from the colour map of the contour plots, all the actuators feature a similar momentum deficit at the same number of D^* behind the actuators. The regions with equivalent frontal area, however, does feature an asymptotic development towards circular wake. Consequently, the AR of the shear layer becomes less at $6D^*$, while constantly decreased perimeters are also observed. A quantitative discussion is available in the next section.

4.3. Mean streamwise velocity deficit normalisation

A comparison of the normalised mean streamwise velocity deficit along the x-coordinate is presented in Fig. 14, where $\Delta U/U_\infty = 1 - U/U_\infty$, to validate the effective mixing diameter D^*. The velocity deficit is averaged within the upper half of the cross-sections, to avoid any effect form the support's wake. Three normalisation lengths in the literature, namely width W (corresponding to rotor diameter D when representing wind turbines), characteristic length $l = A^{1/2}$, and equivalent diameter $D_{eq} = (4WH/\pi)^{1/2}$, together with the concept of the effective mixing diameter D^* proposed in this work, are compared. l and D_{eq} are incorporated in one graph.

When the data are normalised with W, as shown in Fig. 14, the rectangular actuator features the lowest recovery rate. However, the latter can be rather considered as an artefact of the normalisation choice, as the actuator width is also the shortest length among those used in all criteria.

When the data takes into account the overall cross-section (the equivalent diameter scaling, D_{eq}, [22]; and characteristic length, l), the rectangular actuator features the fastest recovery. Considering the fact that non-circular-symmetric actuators exhibit longer perimeter than circular-symmetric ones, the latter indicates that for a chosen cross-sectional area, the longer the perimeter the higher is the momentum recovery rate. Despite of a coefficient of $(4/\pi)^{1/2}$, l and D_{eq} are actually based on the same principle. The differences are that the former transforms the wake generator to an equivalent square, whereas the latter transforms it to an equivalent circle.

Including the perimeter of the deficit region in the normalisation (D^*), a more unified behaviour is observed for the three

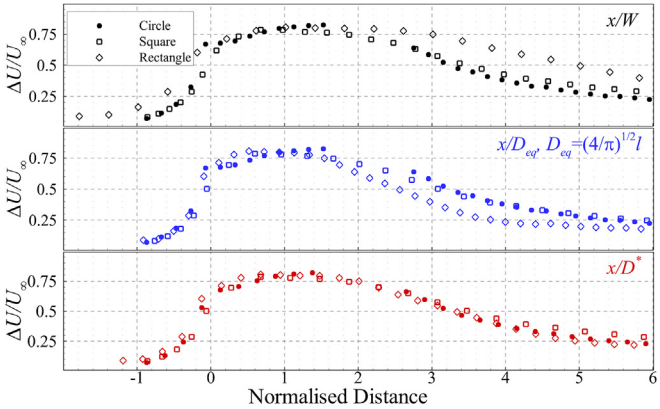

Fig. 14. Comparison of streamwise velocity deficit averaged in the upper half of the projected area along x-direction (downstream distance normalised by W, $D_{eq}(l)$, D^*).

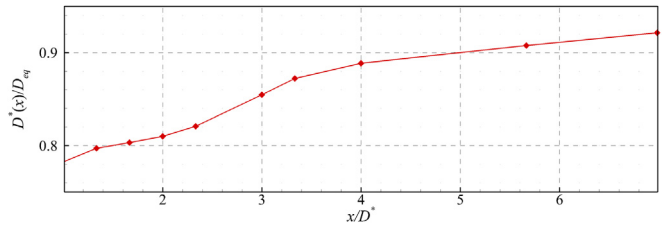

Fig. 15. Wake *circularity* ($D^*(x)/D_{eq}$) evolution along x/D^* for the rectangular actuator.

considered cases as the curves of the streamwise velocity deficit development collapse to a better extent.

To examine how the actuator wake shape departs from the circular assumption and how it evolves towards it, the evolution of the wake *circularity* given by the ratio $D^*(x)/D_{eq}$ is presented in Fig. 15 for the rectangular actuator. $D^*(x)$ is evaluated at each section along x, using the perimeter of deficit area, which is equivalent to the actuator frontal area. The wake will eventually become circular [26], corresponding to condition $D^*/D_{eq} = 1$. Fig. 15 indicates such asymptotic behaviour, and the aforementioned normalisation comparison shows that when $D^*(x)/D_{eq} > 0.9$ (corresponding to $x/D^* > 5$), the wake normalisation based on D^* and D_{eq} are equivalent. The latter is also supported in Fig. 14, by a good collapse of the data for D_{eq} at a distance beyond 5 equivalent diameters.

5. D^* normalisation for VAWT wakes

In this section, numerical simulations are conducted to assess the validity of the D^* normalisation for the scaling of the wakes of VAWTs with different aspect ratios.

5.1. Numerical simulations

The simulated VAWTs are based on the geometry investigated and reported by Ref. [38]; with the exception that the struts and the supporting towers are not included, for sake of simplicity. For the purpose of verifying the normalisation based on the D^* concept, a set of simulations covering VAWTs with values of AR varying in the range {1,2,3,10} were carried out. The rotor diameter was kept constant, while the height was varied. All simulations have the same inflow conditions and mesh density/topology. A schematic of the simulation domain is presented in Fig. 16, where VAWTs with AR of 1 (solid black) and 3 (dashed blue) are illustrated. The dimensions of the computational domain are comparable with those reported by Ref. [39]. In particular, with varying VAWT height, the height of the simulation domain is also varied such to keep a constant ratio of 7 between the simulation domain and the VAWT heights.

Moreover, for the case of AR = 10, the downstream domain is extended to 20D, so as to enable a comparison with the D_{eq}-based scaling (Figs. 18 and 19). All the turbines rotate with the same tip speed ratio of 4.5, similar to the cases of Shamsoddin and Porté-Agel [22], to achieve the same centre plane C_T (0.92). The tip loss effect causing a decreased overall C_T especially at small AR is omitted in the comparison. The resulting overall wind turbine thrust coefficients are listed in Table 3 for all the cases.

The numerical simulation was carried out with the actuator line model (ALM) coupled with a dynamic stall model (DSM), using the flow velocity from the Navier-Stokes solver and then determining the angle of attack and relative velocity to solve the blade forces. The forces are therefore used as representative of those exerted by the VAWT. The flow field was simulated with the OpenFOAM open-source CFD framework, by solving URANS equations and the k-ε turbulence model.

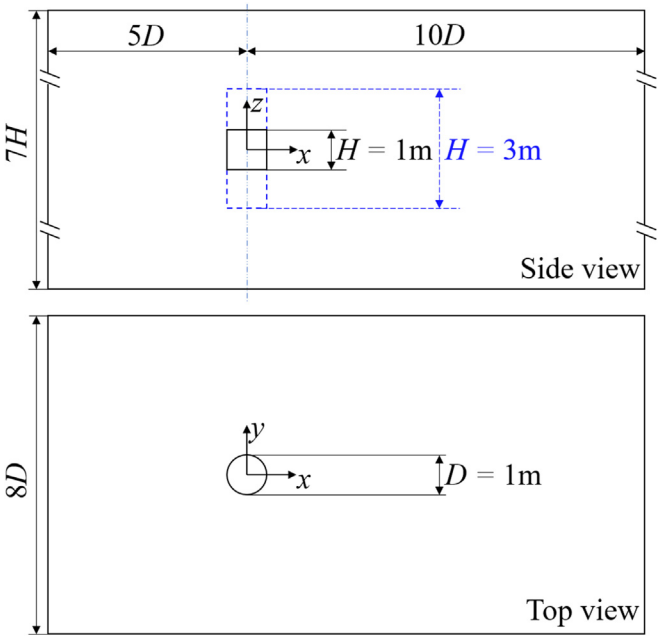

Fig. 16. Schematic of the numerical simulation domain with variable height. VAWTs with AR = {1, 3} are presented.

Table 3
Thrust coefficients of the VAWTs with AR = {1, 2, 3, 10}.

AR	C_T
1	0.75
2	0.81
3	0.82
10	0.91

The *turbinesFoam* library developed by Bachant and Wosnik [25]; which consists of the ALM and DSM, was used for the numerical experiment implementation. The library together with the OpenFOAM framework has been extensively validated and reported in the literature. Nevertheless, a case specific validation, using the same domain topology is presented here, setting flow conditions according to Ref. [38] and including the struts and shaft. Furthermore, the results are compared to LES simulation data for the same case produced by the same OpenFOAM library [39].

The simulated mean streamwise velocity profiles along horizontal and vertical planes crossing the turbine centre are compared in Fig. 17. The comparison shows that the present URANS simulation reproduces the mean velocity field in agreement with existing experimental and numerical investigations. Local discrepancies are limited within 15% of the free-stream value compared to the experimental data. The comparison of the normalisation methods reported hereafter is based on the cross-sectional average of the velocity, which further decreases the value of such discrepancies to within 8%.

5.2. Comparison of wake normalisation

The velocity deficit evolution downstream of the turbine locations is presented in Fig. 18, comparing rotors of different AR. As expected, for a fixed value of the rotor diameter, the larger the AR (cross-sectional area), the longer the wake persists, with a significant increment observed when transitioning from the square cross-section to the turbine with AR = 2.

The velocity deficit evolving along the wake is represented again with the downstream distance normalised by a relevant length

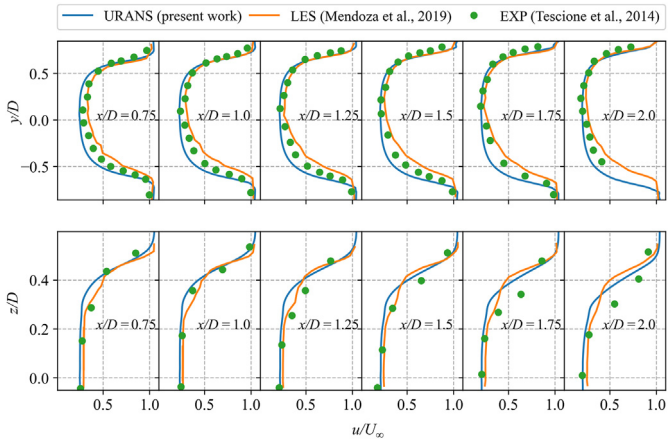

Fig. 17. Comparison of horizontal (top) and vertical (bottom) profiles of normalised mean streamwise velocity along the x-direction. Blue lines: the URANS simulation results from the present work; Green dots: the experimental data of Tescione et al. [38]; Orange lines: the large eddy simulation (LES) results from Mendoza et al. [34].

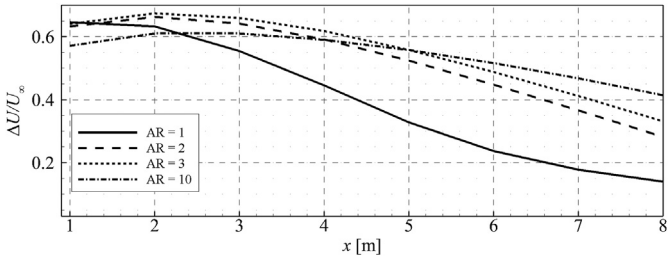

Fig. 18. Comparison of streamwise velocity deficit (averaged over the projected area) along x-direction in the wake of VAWTs with AR = {1, 2, 3, 10}. The VAWT diameter is $D = 1$ m.

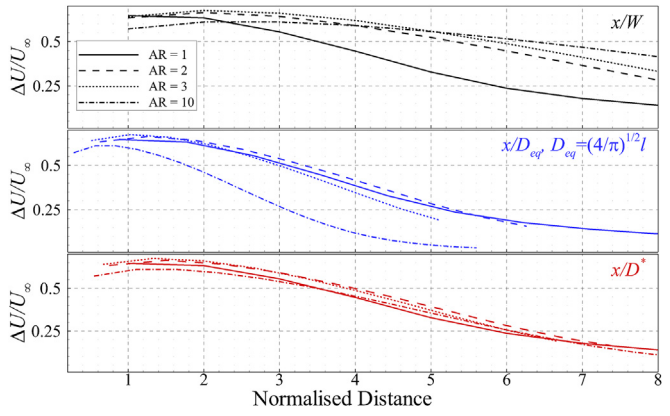

Fig. 19. Comparison of streamwise velocity deficit (averaged over the projected area) along x-direction. Data are normalised by D, $D_{eq}(l)$, D^* in the wake of VAWTs with AR = {1, 2, 3, 10}.

scale. A comparison of the velocity deficit considering the aforementioned normalisation lengths (namely D (or W), $D_{eq}(l)$, and D^*) is depicted in Fig. 19, over the chosen range of AR. It is expected that the normalisation taking into account the relevant driving mechanisms (imparted momentum deficit at the actuator, momentum exchange rate across the wake interface) would yield a behaviour of the momentum deficit that is less dependent upon the turbine shape, the AR in the present case.

The wake recovery purely based on D (black lines) does not take into account the increase of cross-sectional area with AR and therefore, the recovery appears to become slower for increasing values of AR.

In the case of $D_{eq}(l)$, when the turbine cross-sectional shape becomes elongated, the normalising length scale is increased, which results in underpredicting the recovery length. As a result, still a significant spreading of the normalised curves is observed in the data.

The normalisation by D^* (red lines) accounts for the equivalent cross-sectional area (initial momentum deficit imparted by the actuator) as well as for the actuator perimeter (momentum exchange rate across the effective wake interfacial area). The normalised wake deficit based on D^* significantly reduces the wake recovery dependency on the AR, indicating the suitability for the general treatment of VAWT wake of arbitrary shape.

6. Conclusions

The effects of actuator shape, specifically the aspect ratio of rectangular ones, on the scaling of the wake recovery have been investigated by means of experiments and simulations. A theoretical derivation of the effective mixing diameter D^*, based on momentum conservation, is provided. The resulting D^* is proportional to the ratio between the actuator's area and its perimeter (in analogy to the hydraulic diameter), and is proposed as a characteristic length to better represent the wake recovery of actuators of different shapes. Three-dimensional data collected in the wake of circular, square and rectangular actuators, obtained from plates of uniform porosity, are used to validate the proposed formulation of D^*, as well as to expand the fundamental knowledge of the frontal shape effects of actuator surfaces. The results of Figs. 14 and 19 confirm that, in spite of the approximation made in the definition of the control volume that accounts for the actuator's perimeter and not for the actual shear layer's perimeter, the use of D^* provides a better agreement among the velocity deficits of different actuator surfaces up to a normalised streamwise distance of 8.

Although the velocity measurements return clear edge effects at the corner of the square and rectangular actuators, thrust measurements with a load sensor indicated that the C_T is not sensitive to the shape of the planar actuator (confirming the independence of streamtube used in BEM theory), and the related edge effects. Nevertheless, the downstream development of the momentum deficit features a significant distortion induced by such edge effects. In particular, a lower rate of expansion at the corners is observed; the latter is caused by streamwise vortex-pairs that induce inward motions.

The proposed normalisation length D^* is compared with the recently proposed equivalent diameter D_{eq} from Ref. [22]; a commonly used characteristic length l, and the width W (or diameter D) that is frequently used in kinematic wake models as a scaling parameter. When the latter quantities are used as scaling parameters, the wake recoveries from actuators of different ARs depart considerably from each other. Conversely, when a spatial normalisation by D^* for the streamwise direction is taken, a better agreement is observed between the velocity deficit for different actuator shapes.

Furthermore, D^* is used for the normalisation of VAWT wake as a proof of concept. A good agreement among the wakes of VAWTs with different aspect ratios indicates D^* as a promising normalisation criterion.

CRediT authorship contribution statement

Ming Huang: Conceptualization, Methodology, Validation, Formal analysis, Methodology, Investigation, Writing – original draft, Writing – review & editing, Visualization. **Carlos Ferreira:** Conceptualization, Methodology, Resources, Writing – review &

Table 4
Experimental parameters for robotic and planar PIV measurements.

		Robotic PIV	Planar PIV
Seeding	• Tracer particle	Helium-filled soap bubbles	Water-glycol particles
	• Particle size	400 μm	1 μm 1×
	• Particle density	1.2 kg/m^3	10^3 kg/m^3
Illumination	• Pulse energy	50 mJ	2 × 200 mJ
	• Wavelength	527 nm	532 nm
	• IFOV	A pyramid which extends from 8 × 13 cm^2 to 25 × 40 cm^2, with a height of 40 cm	2 mm thick sheet of 210(H) × 280(W) mm^2
Optics	• Focal length	4 × 4 mm	65 mm
	• Numerical aperture	8	11.2
Imaging	• Tomographic aperture	4° at 40 cm away from the camera plane	–
	• Active sensor	512 × 500 px	1628 × 1236 px
	• Pixel pitch	4.8 μm	4.4 μm
	• Acquisition frequency	789 Hz	5 Hz
Post processing	• Window/bin size	20 × 20 × 20 mm^3	64 × 64 px (11 × 11 mm^2)
	• Overlap	75%	75%
	• Vector pitch	5 mm	2.25 mm

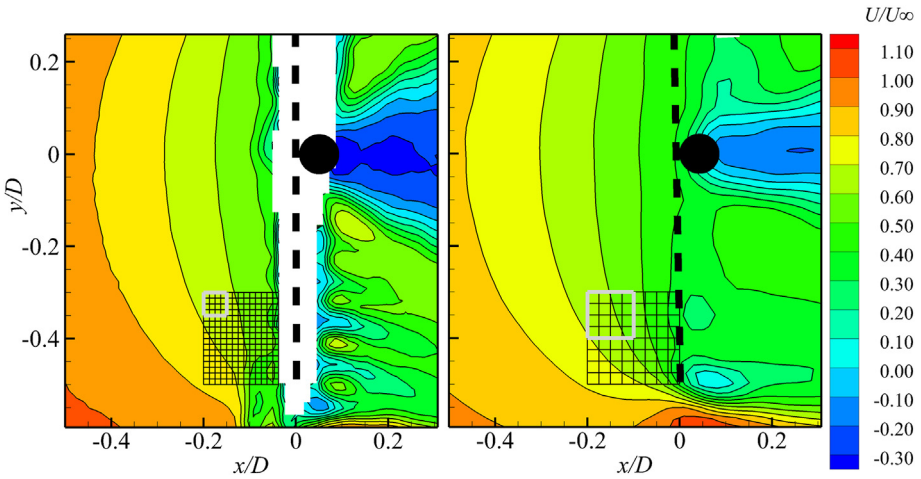

Fig. 20. Colour contours of the time-averaged and normalised streamwise velocity of the circular actuator in the x-y plane at $z/D = 0$. Measurements by planar (left) and robotic PIV (right). The grid in the bottom-right corner indicates the vector data spacing in the measurement, the grey grids indicate the window/bin size.

editing, Validation. **Andrea Sciacchitano:** Conceptualization, Methodology, Validation, Formal analysis, Writing – review & editing, Resources. **Fulvio Scarano:** Conceptualization, Methodology, Validation, Writing – review & editing, Resources.

Declaration of competing interest

The authors declare that they have no known competing financial interests or personal relationships that could have appeared to influence the work reported in this paper.

Acknowledgments

The present research is partly supported by the China Scholarship Council, grant number: CSC No. 201806290006. The first author sincerely appreciates Dr. Yu Zhang for proof reading and polishing parts of the article.

Appendix A

This appendix presents a comparison between robotic PIV and planar PIV measurements. A Quantel *Evergreen* double-pulsed Nd:YAG laser produces pulses with 200 mJ energy at a wavelength of 532 nm within a laser sheet of approximately 2 mm width. A SAFEX smoke generator releases water-glycol seeding particles of average 1 μm diameter. The seeding particles convected through the test section are imaged by a LaVision *Imager LX 2 MP* camera (10-bit, image resolution of 1628 px × 1236 px, pixel pitch of 4.4 μm). The field of view extends from 0.5D upstream to 0.3D downstream. The experiments are conducted with the circular porous plate. The comparison of the robotic PIV and the planar PIV measurement parameters is listed in Table 4.

The velocity fields measured by the planar and robotic PIV, along with the windows/bins are compared in Fig. 20. The results return excellent agreement upstream of the plate. For instance, at $y/D = 0$, and x/D from - 0.5D to - 0.1D, the relative error of the velocity is approximately 1.3%. Differences can be observed immediately downstream of the disc, where the alternate patterns of high velocity through the pore and separated flow after the solid portion of the mesh can be appreciated with the higher resolution of planar PIV. By contrast, the velocity field measured by robotic PIV returns a spatially averaged value in the close proximity of the plate.

Appendix B

Supplementary data for the plots and the scripts of the models discussed in this article can be found at https://doi.org/10.4121/12923897.

References

[1] J. Bossuyt, C. Meneveau, J. Meyers, Wind farm power fluctuations and spatial sampling of turbulent boundary layers, J. Fluid Mech. 823 (2017) 329–344.
[2] S. Aubrun, S. Loyer, P.E. Hancock, P. Hayden, Wind turbine wake properties: comparison between a non-rotating simplified wind turbine model and a rotating model, J. Wind Eng. Ind. Aerod. 120 (2013) 1–8.
[3] M.F. Howland, J. Bossuyt, L.A. Martínez-Tossas, J. Meyers, C. Meneveau, Wake structure in actuator disk models of wind turbines in yaw under uniform inflow conditions, J. Renew. Sustain. Energy 8 (2016), 043301.
[4] L.E.M. Lignarolo, D. Ragni, C.J. Ferreira, G.J.W. van Bussel, Experimental comparison of a wind-turbine and of an actuator-disc near wake, J. Renew. Sustain. Energy 8 (2016), 023301.
[5] S. de J. Helvig, M.K. Vinnes, A. Segalini, N.A. Worth, R.J. Hearst, A comparison of lab-scale free rotating wind turbines and actuator disks, J. Wind Eng. Ind. Aerod. (2021) 209.
[6] I.P. Castro, Wake characteristics of two-dimensional perforated plates normal to an air-stream, J. Fluid Mech. 46 (1971) 599–609.
[7] K. Steiros, M. Hultmark, Drag on flat plates of arbitrary porosity, J. Fluid Mech. 853 (R3) (2018) 1–11.
[8] A.E. Craig, J.O. Dabiri, J.R. Koseff, Low order physical models of vertical axis wind turbines, J. Renew. Sustain. Energy 9 (2017) 1–17.
[9] R. Fail, J.A. Lawford, R.C.W. Eyre, Aeronaut. Res. Counc. Reports Memo. 3120 (1957) 1–21.
[10] D. Medici, P.H. Alfredsson, Wind turbine near wakes and comparisons to the wake behind a disc, in: 43rd AIAA Aerospace Sciences Meeting and Exhibit - Meeting Papers, American Institute of Aeronautics and Astronautics Inc, 2005, pp. 15593–15604.
[11] R.J.A.M. Stevens, C. Meneveau, Flow structure and turbulence in wind farms, Annu. Rev. Fluid Mech. 49 (2017) 311–339.
[12] T. Göçmen, P. Van Der Laan, P.E. Réthoré, A.P. Diaz, G.C. Larsen, S. Ott, Wind turbine wake models developed at the technical university of Denmark: a review, Renew. Sustain. Energy Rev. 60 (2016) 752–769.
[13] F. Porté-Agel, M. Bastankhah, S. Shamsoddin, Wind-turbine and wind-farm flows: a review, Boundary-Layer Meteorol. 174 (2020) 1–59.
[14] N.O. Jensen, in: -M. Risø (Ed.), A Note on Wind Generator Interaction, No.2411, Risø National Laboratory, Roskilde, 1983.
[15] G.C. Larsen, A simple wake calculation procedure, in: Risø-M, No. 2760, Risø National Laboratory, 1988.
[16] M. Bastankhah, F. Porté-Agel, A new analytical model for wind-turbine wakes, Renew. Energy 70 (2014) 116–123.
[17] H. Tennekes, J.L. Lumley, A First Course in Turbulence, MIT Press, 1972.
[18] M. Abkar, Theoretical modeling of vertical-Axis wind turbine wakes, Energ. 12 (2018) 10.
[19] M. Abkar, J.O. Dabiri, Self-similarity and flow characteristics of vertical-axis wind turbine wakes: an LES study, J. Turbul. 18 (2017) 373–389.
[20] H.F. Lam, H.Y. Peng, Development of a wake model for Darrieus-type straight-bladed vertical axis wind turbines and its application to micro-siting problems, Renew. Energy 114 (2017) 830–842.
[21] J. Nedić, O. Supponen, B. Ganapathisubramani, J.C. Vassilicos, Geometrical influence on vortex shedding in turbulent axisymmetric wakes, Phys. Fluids 27 (2015), 035103.
[22] S. Shamsoddin, F. Porté-Agel, Effect of aspect ratio on vertical-axis wind turbine wakes, J. Fluid Mech. 889 (2020) R1 1–R12.
[23] R.J.A.M. Stevens, D.F. Gayme, C. Meneveau, Effects of turbine spacing on the power output of extended wind-farms, Wind Energy 19 (2016) 359–370.
[24] C. Jux, A. Sciacchitano, J.F.G. Schneiders, F. Scarano, Robotic volumetric PIV of a full-scale cyclist, Exp. Fluid 59 (2018) 74.
[25] P. Bachant, M. Wosnik, Characterising the near-wake of a cross-flow turbine, J. Turbul. 16 (2015) 392–410.
[26] M. Boudreau, G. Dumas, Comparison of the wake recovery of the axial-flow and cross-flow turbine concepts, J. Wind Eng. Ind. Aerod. 165 (2017) 137–152.
[27] P. Mycek, B. Gaurier, G. Germain, G. Pinon, E. Rivoalen, Experimental study of the turbulence intensity effects on marine current turbines behaviour. Part I: One single turbine, Renew. Energy 66 (2014) 729–746.
[28] H. Darcy, Recherches expérimentales relatives au mouvement de l'eau dans les tuyaux, in: Mallet-Bachelier, 1857, p. 268, and atlas)Paris.
[29] J.F.G. Schneiders, F. Scarano, C. Jux, A. Sciacchitano, Coaxial volumetric velocimetry, Meas. Sci. Technol. 29 (2018), 065201.
[30] D.E. Faleiros, M. Tuinstra, A. Sciacchitano, F. Scarano, Generation and control of helium-filled soap bubbles for PIV, Exp. Fluid 60 (2019).
[31] A. Sciacchitano, F. Scarano, Elimination of PIV light reflections via a temporal high pass filter, Meas. Sci. Technol. 25 (2014), 084009.
[32] D. Schanz, S. Gesemann, A. Schröder, Shake-The-Box: Lagrangian particle tracking at high particle image densities, Exp. Fluid 57 (2016) 70.
[33] A. Betz, Schraubenpropeller mit geringstem Energieverlust. Mit einem Zusatz von l. Prandtl, Nachrichten von Der Gesellschaft Der Wissenschaften Zu Göttingen, Math. Klasse, 1919, pp. 193–217, 1919.
[34] W. Yu, C. Ferreira, G.A.M. van Kuik, The dynamic wake of an actuator disc undergoing transient load: a numerical and experimental study, Renew. Energy 132 (2019) 1402–1414.
[35] S. Aubrun, M. Bastankhah, R.B. Cal, B. Conan, R.J. Hearst, D. Hoek, M. Hölling, M. Huang, C. Hur, B. Karlsen, A. Zasso, Round-robin tests of porous disc models, in: Journal of Physics: Conference Series, vol. 1256, IOP Publishing, 2019.
[36] F. Pierella, L. Saetran, Wind tunnel investigation on the effect of the turbine tower on wind turbines wake symmetry, Wind Energy 20 (2017) 1753–1769.
[37] J. Nedić, B. Ganapathisubramani, J.C. Vassilicos, Drag and near wake characteristics of flat plates normal to the flow with fractal edge geometries, Fluid Dynam. Res. 45 (2013), 061406.
[38] G. Tescione, D. Ragni, C. He, C.J. Simão Ferreira, G.J.W. Van Bussel, Near wake flow analysis of a vertical axis wind turbine by stereoscopic particle image velocimetry, Renew. Energy 70 (2014) 47–61.
[39] V. Mendoza, P. Bachant, C. Ferreira, A. Goude, Near-wake flow simulation of a vertical axis turbine using an actuator line model, Wind Energy 22 (2019) 171–188.